Catalysis Science & Technology

ROYAL SOCIETY OF CHEMISTRY

PAPER

View Article Online
View Journal | View Issue

Cite this: *Catal. Sci. Technol.*, 2023, **13**, 4534

Mg-doped $SrTiO_3$ photocatalyst with Ag–Co cocatalyst for enhanced selective conversion of CO_2 to CO using H_2O as the electron donor†

Takechi Nakamoto, [a] Shoji Iguchi, *[a] Shimpei Naniwa, [a] Tsunehiro Tanaka [ab] and Kentaro Teramura *[abc]

Received 27th April 2023,
Accepted 4th July 2023

DOI: 10.1039/d3cy00576c

rsc.li/catalysis

Photocatalytic conversion of CO_2 by H_2O is a promising method for solving energy and environmental problems. In this context, efficient photocatalysts that facilitate the selective conversion of CO_2 to the value-added chemical CO are essential. In this study, for the first time in the literature, we used an Mg-doped $SrTiO_3$ photocatalyst (Mg–$SrTiO_3$) for the photocatalytic conversion of CO_2 to CO using H_2O as the electron donor under monochromatic UV-light irradiation at 365 nm. Compared to pristine $SrTiO_3$, Mg–$SrTiO_3$, which was prepared *via* a flux method, exhibited dramatically enhanced conversion of CO_2 to CO in the presence of an Ag–Co cocatalyst. Moreover, the selectivity toward CO evolution was >99%, which indicates suppression of the unnecessary and competitive H_2 evolution. Scanning electron microscopy of Mg–$SrTiO_3$ revealed edge-shaved cubic particles, which were correlated to the anisotropic distribution of photogenerated electrons and holes and the consequent enhancement of photocatalytic activity. Furthermore, the Mg-doping temperature and amount used to prepare Mg–$SrTiO_3$ influenced the substitution of Ti^{4+} sites by Mg^{2+} in the bulk of $SrTiO_3$, thereby affecting the CO evolution. The apparent quantum efficiency of optimal Mg–$SrTiO_3$ in the photocatalytic conversion of CO_2 was determined to be 0.05%.

Introduction

Climate change is a serious and escalating problem globally.[1,2] It is primarily attributed to the greenhouse effect of atmospheric CO_2.[3] The concentration of atmospheric CO_2 reached over 400 ppm by 2013 and has been predicted to further increase in the near future.[4] Among the many approaches to reduce CO_2 emissions,[5–7] photocatalysis has attracted significant attention owing to several reasons.

In 1972, Honda and Fujishima reported that photoirradiation of TiO_2 electrodes can shift the anode potential for water oxidation in electrochemical water splitting to a more negative value.[8] This study promoted the development of photocatalysis for degradation of organic compounds and overall water splitting. A promising photocatalyst that is widely used for generating clean energy is the perovskite oxide $SrTiO_3$.[9–12] Domen *et al.* reported that Al-doped $SrTiO_3$ (Al–$SrTiO_3$) is an excellent photocatalyst for efficient photocatalytic H_2O splitting,[13] where it showed a near 100% internal quantum efficiency. This efficiency was attributed to the particle shape of the photocatalyst, which promotes charge separation, as evidenced by an electrical simulation.[14] Yamakata *et al.* demonstrated that doping Na^+ into $SrTiO_3$ improved the photocatalytic activity for water splitting. They concluded that the generated oxygen vacancies act as trapping sites for the photogenerated electrons, consequently extending their lifetimes.[15,16]

Even though photocatalytic water splitting has been extensively studied, the photocatalytic conversion of CO_2 by water, which is known as "artificial photosynthesis", requires further improvement.[17–19] Conversion of the emitted CO_2 into value-added chemicals such as CO, HCOOH, CH_3OH, and CH_4 using solar light could promote a sustainable society built on energy recycling.[20,21] In particular, CO is considered as a useful and important product, as it can be

[a] *Department of Molecular Engineering, Graduate School of Engineering, Kyoto University, Kyoto-daigaku Katsura, Nishikyo-ku, Kyoto 615-8510, Japan. E-mail: iguchi.shoji.4k@kyoto-u.ac.jp, teramura.kentaro.7r@kyoto-u.ac.jp; Fax: +81 75 383 2561; Tel: +81 75 383 2559*

[b] *Elements Strategy Initiative for Catalysts & Batteries (ESICB), Kyoto University, 1-30 Goryo-Ohara, Nishikyo-ku, Kyoto 615-8245, Japan*

[c] *Fukui Institute for Fundamental Chemistry, Kyoto University, Takano Nishibiraki-cho 34-4, Sakyo-ku, Kyoto 606-8103, Japan*

† Electronic supplementary information (ESI) available: XRD patterns and UV-vis DRS of M–$SrTiO_3$, reaction results over Ag–Co/Mg–$ATiO_3$, Mg 2p XPS spectra of Mg–$SrTiO_3$, Ag K-edge XANES spectra, TEM images of Ag or Co-loaded Mg–$SrTiO_3$ (PD), reaction results over Ag–Co/Mg–$SrTiO_3$ (CR, PD, and IMP), particle diameter distributions of Ag, reaction results over MgO-loaded $SrTiO_3$ and Al–$SrTiO_3$, SEM image of Mg–$SrTiO_3$_1118 K, XRD patterns and reaction results of Mg–$SrTiO_3$_***y*** h, XRD patterns of Mg(*z*)–$SrTiO_3$, actual atomic content of Mg–$SrTiO_3$, Mg–$SrTiO_3$_1268 K, and Mg(2)–$SrTiO_3$, results of control experiments, a time-course reaction result, diameter of Ag to photoirradiation time, scheme of reaction system, the calculation of AQE. See DOI: https://doi.org/10.1039/d3cy00576c

converted into a liquefied hydrocarbon, which is a raw material in core industries, through the Fischer–Tropsch process.[22] Our research group has previously reported the photocatalysts Ag/SrO/Ta_2O_5, Ag/$La_2Ti_2O_7$, Ag/$ZnTa_2O_6$, and Ag/$SrNb_2O_6$ for the selective conversion of CO_2 by water under UV-light irradiation (<300 nm).[23–26] These photocatalysts use water as both an electron donor and a proton source, which is favourable because water is abundant, cheap, easy to use, and non-toxic. Moreover, we demonstrated that Ag/$Sr_2KTa_5O_{15}$ and Ag/$ZnGa_2O_4$/Ga_2O_3 facilitated a sufficiently high selectivity toward CO_2 conversion *via* the complete suppression of H_2 evolution.[26,27] Even though H_2 evolution (H^+/H_2: −0.41 V *vs.* NHE at pH = 7.0) proceeds preferentially over CO_2 reduction owing to the more negative standard redox potential of the latter reaction (CO_2/CO: −0.51 V *vs.* NHE at pH = 7.0),[28] the modification of photocatalysts with appropriate cocatalysts enabled selective CO formation.[29–31] Furthermore, a recent study reported that, Ag–Co/Al–$SrTiO_3$ is the most effective photocatalyst for the photocatalytic conversion of CO_2 under an irradiation of 365 nm.[32] This was attributed to the bandgap energy of Al-doped $SrTiO_3$ (3.2 eV), which is smaller than those of the previously reported Ga-based and Ta-based photocatalysts.[33–35] The Ag–Co dual cocatalyst was more effective than single Ag and Co cocatalysts for CO evolution when paired with Al–$SrTiO_3$, where Ag and Co are active sites for CO_2 conversion and H_2O oxidation, respectively.[36,37] The formation rate of CO over Ag–Co/Al–$SrTiO_3$ was approximately seven times higher than that of Ag/Al–$SrTiO_3$.[32,38] In a continuation of our efforts to identify effective photocatalysts for the photocatalytic conversion of CO_2 to CO in water, in this study, we investigated metals other than Al as dopants for $SrTiO_3$ and optimized the doping process. Subsequently, we evaluated the photocatalytic activity of the doped $SrTiO_3$ photocatalysts in the conversion of CO_2 to CO under UV-LED-light irradiation at 365 nm.

Experimental section

Preparation of the photocatalysts

The perovskite-structured $SrTiO_3$ photocatalyst was fabricated *via* a previously reported solid-state method.[39] $SrCO_3$ (21 mmol) and TiO_2 (20 mmol) were ground for 15 min using a mortar and pestle, and the mixture was transferred to an alumina crucible to calcine at 1373 K for 10 h in air. The resulting powder was washed three times with hot ultrapure water and dried overnight at room temperature. $BaTiO_3$ and $CaTiO_3$ were synthesised *via* the same procedure using $BaCO_3$ and $CaCO_3$ as precursors, respectively.

M-doped $SrTiO_3$ (M–$SrTiO_3$, M = Al, Zn, Li, Mn, W, Ca, Y, and Mg) was synthesised *via* a flux method.[36] $SrCl_2$ flux (100 mmol) was added to a mixture of the prepared $SrTiO_3$ (10 mmol) and a metal oxide (0.4 mmol). The mixture was ground for 15 min using a mortar and pestle, transferred to an yttria crucible, and calcined at 1418 K for 15 h. The obtained powder was washed three times with hot ultrapure water and dried overnight at 353 K. Next, we fabricated a series of Mg–$SrTiO_3$ photocatalysts, termed as Mg–$SrTiO_3$_***x*** K, Mg–$SrTiO_3$_***y*** h, and Mg(***z***)–$SrTiO_3$, where ***x***, ***y***, and ***z*** are the calcination temperature (***x*** = 1118, 1268, 1318, 1368, and 1418 K), calcination time (***y*** = 1, 10, 15, and 20 h), and molar ratio (mol%) of Mg to Ti (***z*** = 0, 2, 4, 8, 24, and 100), respectively. Mg-doped $BaTiO_3$ (Mg–$BaTiO_3$) and Mg-doped $CaTiO_3$ (Mg–$CaTiO_3$) were also fabricated *via* the same method using $BaCl_2$ and $CaCl_2$ as fluxes, respectively.

Loading of the cocatalysts

A conventional chemical reduction (CR) method was used to load Ag and Co cocatalysts onto the surface of M–$SrTiO_3$.[36] M–$SrTiO_3$ (0.75 g) was dispersed in ultrapure water (50 mL), and the suspension was maintained at 353 K. Aqueous solutions of $AgNO_3$ (0.1 M, 0.695 mL), $Co(NO_3)_2$ (0.1 M, 0.347 mL), and NaH_2PO_2 (0.4 M, 1.5 mL) were added to the suspension while continuously stirring. The resultant suspension was maintained at 353 K for 1.5 h. The solid residue was collected *via* vacuum filtration and dried overnight at room temperature to obtain the Ag–Co/M–$SrTiO_3$ powder.

Furthermore, MgO/$SrTiO_3$ and MgO/Al–$SrTiO_3$ were prepared *via* an impregnation method as reference materials.[32] $SrTiO_3$ or Al–$SrTiO_3$ (0.92 g) was added to an acetone solution of $Mg(NO_3)_2{\cdot}6H_2O$ (0.051 g). The solvent was completely evaporated by heating the suspension while vigorously stirring, and the resultant powder was calcined at 773 K for 5 h.

Characterization

The crystalline properties of the fabricated photocatalysts were evaluated by X-ray diffraction (XRD) using a Rigaku SmartLab SE equipped with CuKα radiation (λ = 0.154 nm). UV-visible diffuse reflectance spectroscopy (UV-vis DRS) was performed using the JASCO V-670 spectrometer equipped with an integrating sphere. A $BaSO_4$ plate was used as a standard reflection sample. Scanning electron microscopy (SEM) images were obtained at an acceleration voltage of 3.0 kV using a field-emission scanning electron microscope (SU-8220, Hitachi High-Technologies) equipped with an energy-dispersive X-ray spectroscopy (EDS) unit for elemental mapping. X-ray photoelectron spectroscopy (XPS) was performed by an X-ray photoelectron spectrometer (ESCA 3400, Shimadzu Corp.) at various Ar sputtering times (emission 70 mA; Accel HT: 0.6 kV). Inductively coupled plasma optical emission spectrometry (ICP-OES, iCAP7400, Thermo Fisher Scientific, Inc.) was used to determine the atomic content of Sr, Ti, and Mg in Mg–$SrTiO_3$.

Photocatalytic reactions

The photocatalytic conversion of CO_2 by H_2O as the electron donor was conducted using an external irradiation-type reaction vessel (Scheme S1†) in a quasi-flowing batch system. Ag–Co/M–$SrTiO_3$ (0.2 g) was dispersed in a 0.1 M aqueous solution of $NaHCO_3$ (200 mL). A high purity CO_2 gas (99.999%) was bubbled into the resultant suspension at a flow rate of 60 mL min^{-1} for 1 h to remove the dissolved air in the reaction solution. The suspension was then irradiated

using a monochromatic UV-LED lamp at 365 nm (IRS-1000, CELL System Co., Ltd., Japan) with continuous CO_2 gas flow at a flow rate of 30 mL min^{-1}. The generated gases were analysed using online gas chromatographs equipped with a thermal conductivity detector (TCD-GC; GC-8A, Shimadzu Corporation, Japan; Ar carrier gas; molecular sieve 5A column) and a flame-ionisation detector with a methanizer (FID-GC; GC-8A, Shimadzu Corporation, Japan; N_2 carrier gas; Shincarbon ST column). The CO selectivity and balance of consumed electrons and holes (e^-/h^+) were calculated using eqn (1) and (2) as follows:

$$\text{CO selectivity (\%)} = R_{CO}/(R_{CO} + R_{H_2}) \times 100 \quad (1)$$

$$e^-/h^+ = (2R_{CO} + 2R_{H_2})/4R_{O_2} \quad (2)$$

where R_{CO}, R_{H_2}, and R_{O_2} are the formation rates of CO, H_2, and O_2 (μmol h^{-1}), respectively.

The apparent quantum efficiency (AQE, %) of the photocatalysts was calculated from the formation rate of the product and the light intensity measured using a power meter (OPHIR Photonics, A Newport Company) using eqn (3).

$$\text{AQE (\%)} = (\text{number of reacted electrons/number of incident photons}) \times 100 \quad (3)$$

Number of reacted electrons was calculated using eqn (4) as follows:

$$\text{Number of reacted electrons} = 2 \times (R_{CO} + R_{H_2}) \times 10^{-6} \times N_A \quad (4)$$

where N_A is the Avogadro constant (6.0×10^{23} mol^{-1}).

Results and discussion

Fig. S1† shows the XRD patterns and UV-vis DR spectra of M–$SrTiO_3$ (M = Al, Zn, Li, Mn, W, Ca, Y, or Mg). Well-ordered diffraction patterns corresponding to the perovskite structure were observed in all the cases. Moreover, the dopant metals did not alter the absorption wavelength, whereas the DR spectrum of Mn–$SrTiO_3$ shows a typical absorption corresponding to the d–d transition of the Mn species. Fig. 1 shows the formation rates of gaseous products (CO, H_2, and O_2) and selectivity toward CO evolution in the photocatalytic conversion of CO_2 in the presence of the Ag–Co/M–$SrTiO_3$ photocatalysts (M = Al, Zn, Li, Mn, W, Ca, Y, and Mg) upon photoirradiation for 1 h. Zn–$SrTiO_3$, Li–$SrTiO_3$, Mn–$SrTiO_3$, W–$SrTiO_3$, Ca–$SrTiO_3$, and Y–$SrTiO_3$ exhibited extremely low photocatalytic activities for the conversion of CO_2, whereas Al–$SrTiO_3$ and Mg–$SrTiO_3$ showed moderate activities. Mg–$SrTiO_3$ exhibited the highest activity for CO evolution, which has been observed as a CO formation rate of ~20 μmol h^{-1}. A previous study reported that Al–$SrTiO_3$ showed excellent activity in the presence of Rh/Cr_2O_3/CoOOH cocatalysts during photocatalytic H_2 evolution.[14] However, H_2 evolution was drastically suppressed (0.055 μmol h^{-1}) in the presence

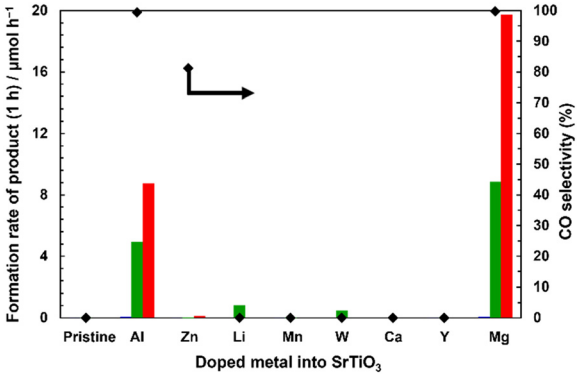

Fig. 1 Formation rates of CO (red), H_2 (blue), and O_2 (green) and the selectivity toward CO evolution (black diamond) in the photocatalytic conversion of CO_2 in H_2O over the pristine and the doped Ag–Co/M–$SrTiO_3$ photocatalysts (M = Al, Zn, Li, Mn, W, Ca, Y, and Mg). Reaction conditions: amount of photocatalyst: 0.2 g; Ag loading: 1 wt%; Co loading: 0.3 wt%; volume of reaction solution (H_2O): 0.2 L; additive: 0.1 M $NaHCO_3$; CO_2 flow rate: 30 mL min^{-1}; light source: monochromatic LED lamp at 365 nm; photoirradiation time: 1 h.

of Ag–Co/Mg–$SrTiO_3$, where the selectivity toward CO evolution was >99%, indicating that Mg-doping into $SrTiO_3$ improved the photocatalytic activity for the conversion of CO_2. Moreover, the CO formation rate over Mg–$SrTiO_3$ was two or more times higher than that over the previously reported Al–$SrTiO_3$ photocatalyst.[32] Furthermore, stoichiometric O_2 evolution (8.9 μmol h^{-1}) was observed in the presence of Mg–$SrTiO_3$ (e^-/h^+ = 1.1), suggesting that H_2O acts as both an electron donor and a proton source for the photocatalytic conversion of CO_2 in water. Fig. S2† shows the photocatalytic activities of Ag–Co/Mg–$ATiO_3$ photocatalysts (A = Ba, Ca, and Sr) in the conversion of CO_2. Mg–$BaTiO_3$ and Mg–$CaTiO_3$ showed extremely low and no photocatalytic activity, respectively, indicating that other perovskite photocatalysts are not effective in this reaction. Therefore, we focused on the effect of Mg-doping into $SrTiO_3$ on the photocatalytic conversion of CO_2 in water.

The XRD patterns of pristine $SrTiO_3$, Mg–$SrTiO_3$, and Ag–Co/Mg–$SrTiO_3$ (Fig. 2(A-1)) correspond to the pure phase of the perovskite structure belonging to the *Pm*3*m* (211) space group (ICSD 23076). Peaks corresponding to the Ag or Co species were not observed in the XRD pattern of Ag–Co/Mg–$SrTiO_3$, suggesting that the Ag–Co cocatalyst was loaded on the surface of Mg–$SrTiO_3$ with high dispersion. The full width at half maximum (FWHM) of the peaks of crystalline $SrTiO_3$, Mg–$SrTiO_3$, and Ag–Co/Mg–$SrTiO_3$ attributed to the (110) phase (2θ = ~32°) were 0.11°, 0.094°, and 0.10°, respectively. Flux treatment during Mg doping resulted in slight crystal growth and enhanced the crystalline character of $SrTiO_3$. However, we believe that these new characteristics of the photocatalyst did not enhance the photocatalytic activity because flux-treated $SrTiO_3$ did not show significant CO evolution in the absence of MgO, as shown in Fig. 6. The peak at approximately 2θ = 67.8° in the pattern of Mg–$SrTiO_3$, shown in Fig. 2(A-2), is ascribed to the (220) phase. This peak

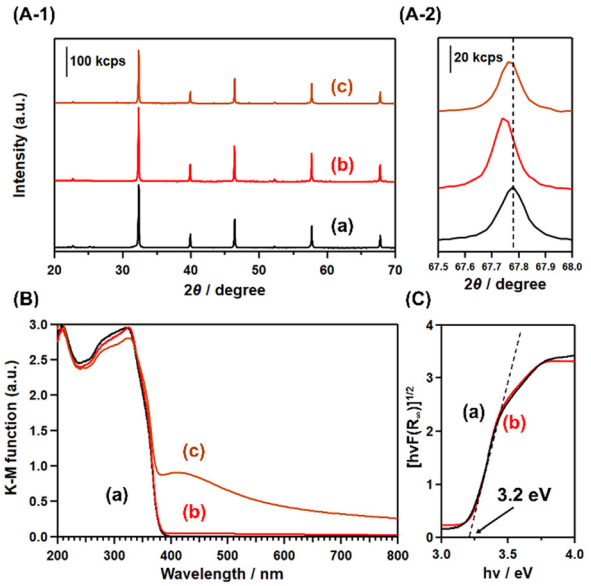

Fig. 2 (A-1) X-ray diffraction (XRD) patterns, (B) UV-visible diffuse reflectance (UV-vis DR) spectra, and (C) Tauc plots of (a) pristine $SrTiO_3$, (b) Mg–$SrTiO_3$, and (c) Ag–Co/Mg–$SrTiO_3$. (A-2) is the magnified view of (a)–(c) in (A-1).

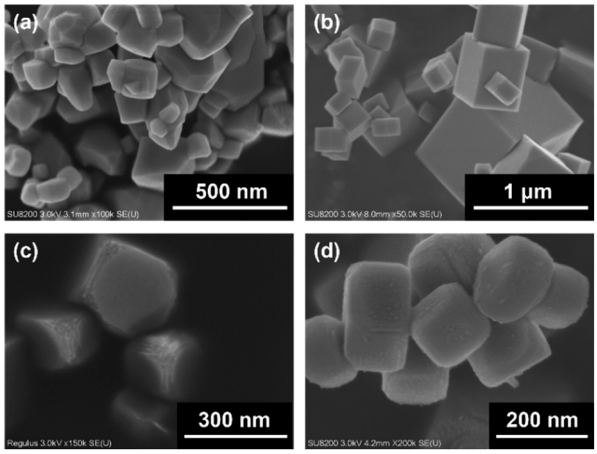

Fig. 3 Scanning electron microscopy (SEM) images of (a) pristine $SrTiO_3$, (b) flux-treated $SrTiO_3$, (c) Mg–$SrTiO_3$, and (d) Ag–Co/Mg–$SrTiO_3$.

shifted to a lower angle than that of $SrTiO_3$, which indicates that replacing Ti^{4+} in the bulk of $SrTiO_3$ with Mg^{2+} dopant extends the lattice plane distance. The ionic radii of six-coordinated Sr^{2+}, Ti^{4+}, and Mg^{2+} were 1.18, 0.605, and 0.720 Å, respectively.[40] Furthermore, the Mg 2p XPS spectra of Mg–$SrTiO_3$ obtained at various Ar sputtering times confirmed that the Mg^{2+} ions were doped into the bulk of $SrTiO_3$ (Fig. S3†).

Fig. 2(B) shows the UV-vis DR spectra of $SrTiO_3$, Mg–$SrTiO_3$, and Ag–Co/Mg–$SrTiO_3$. The absorption edge of $SrTiO_3$ was estimated to be 390 nm, which confirms the suitability of the monochromatized UV-LED irradiation at 365 nm. The UV-vis DR spectrum of Mg–$SrTiO_3$ ((b) in Fig. 2(B)) shows that Mg^{2+} doping did not influence the absorption wavelengths of $SrTiO_3$. The Tauc plot (Fig. 2(C)) revealed that the bandgap energies of pristine $SrTiO_3$ and Mg–$SrTiO_3$ were 3.2 eV, which is consistent with previous reports.[41–43] In the case of Ag–Co/Mg–$SrTiO_3$ ((c) in Fig. 2(B)), a broad absorption was observed in the visible-light region. Typically, Ag demonstrates plasmonic absorption in the visible-light region in its metal form (with a valence number of 0) and in its nanoparticle form. Therefore, we attributed this broad peak to the plasmonic absorption of Ag nanoparticles,[44] which confirms that Ag was loaded on Mg–$SrTiO_3$ in the form of nanoparticles. Moreover, the Ag K-edge XANES spectrum of Ag–Co/Mg–$SrTiO_3$ is in good agreement with that of the Ag foil, indicating that Ag particles with a valence number of 0 were loaded onto Mg–$SrTiO_3$ as a cocatalyst (Fig. S4†).

The SEM image in Fig. 3(a) shows that pristine $SrTiO_3$ has an irregular shape. In the absence of an Mg dopant, the shape of the $SrTiO_3$ particle is regulated by its calcination with $SrCl_2$ flux, resulting in cubic particles with {100} facets (Fig. 3(b)). However, Mg–$SrTiO_3$ has edge-shaved cube particles with {110} facets in addition to the {100} facets, as shown in Fig. 3(c). A similar change was observed for Al–$SrTiO_3$ in previous studies.[13,45] Takata *et al.* have performed calculations to determine the distribution of photogenerated electrons and holes of $SrTiO_3$ in the {100} and {110} facets. They observed that the concentration of electrons around the {100} facets was relatively high, whereas holes were easily transferred to the {110} facets.[4] To confirm this anisotropic charge distribution, we investigated the photodeposition of Ag and Co cocatalysts on the surface of Mg–$SrTiO_3$ in this study. As shown in Fig. S5,† the Ag and Co cocatalysts were deposited on the {100} and {110} facets, respectively. This indicates that photoexcited electrons and holes are selectively distributed in Mg–$SrTiO_3$ based on the facets. This distribution suppresses the electron–hole recombination, thus contributing to the high photocatalytic activity. As mentioned previously, we used the CR method to load Ag and Co cocatalysts on Mg–$SrTiO_3$ as it is regarded as the optimal method for the photocatalytic conversion of CO_2 (Fig. S6†). As shown in Fig. 3(d), the cocatalysts loaded by the CR method were not facet-selective but were highly dispersed on the surface of the Mg–$SrTiO_3$ particles. The average diameter of the Ag cocatalyst was estimated to be 7.0 nm based on the diameter distribution in the transmission electron microscopy (TEM) images. This diameter is smaller than that of the Ag cocatalysts loaded *via* the photodeposition and impregnation methods (Fig. S7†).

Several previous reports have demonstrated that the modification of photocatalysts with metal oxides or hydroxides such as SrO, $Cr(OH)_3$, $Pr(OH)_3$, and layered double hydroxides, which can provide adsorption sites for CO_2, improves the photocatalytic activity in the selective conversion of CO_2.[23,46–50] However, we observed that the CO formation rate and CO selectivity are higher for Mg–$SrTiO_3$ than those for MgO/$SrTiO_3$ and MgO/Al–$SrTiO_3$ (fabricated *via* the conventional impregnation method) in the presence

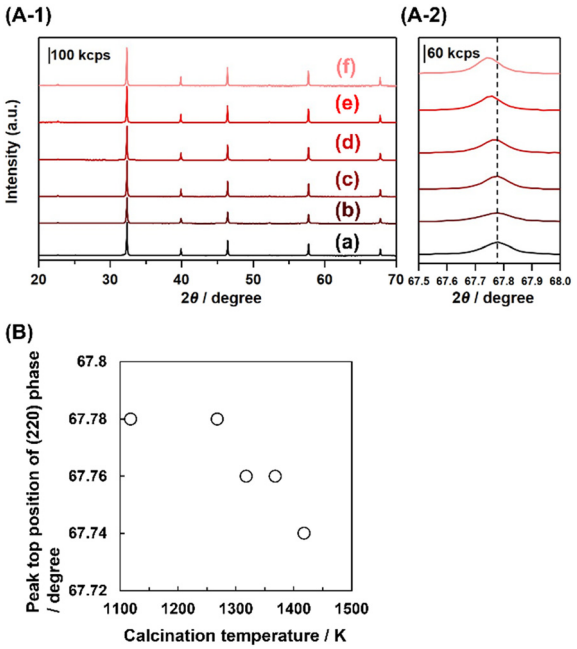

Fig. 4 (A-1) XRD patterns of (a) pristine $SrTiO_3$, (b) Mg–$SrTiO_3$_1118 K, (c) Mg–$SrTiO_3$_1268 K, (d) Mg–$SrTiO_3$_1318 K, (e) Mg–$SrTiO_3$_1368 K, and (f) Mg–$SrTiO_3$_1418 K. (A-2) is the magnified view of (a)–(f) in (A-1). (B) Dependence of calcination temperature on the peak top position of the (220) phase.

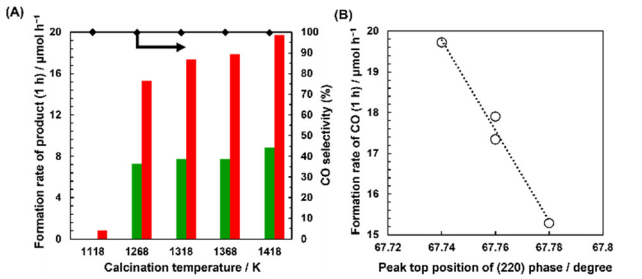

Fig. 5 (A) Formation rates of CO (red), H_2 (blue), and O_2 (green) and the selectivity toward CO evolution (black diamond) in the photocatalytic conversion of CO_2 in H_2O over Ag–Co/Mg–$SrTiO_3$_***x*** K photocatalysts (***x*** = 1118, 1268, 1318, 1368, and 1418). Reaction conditions: amount of photocatalyst: 0.2 g; Ag loading: 1 wt%; Co loading: 0.3 wt%; volume of reaction solution (H_2O): 0.2 L; additive: 0.1 M $NaHCO_3$; CO_2 flow rate: 30 mL min^{-1}; light source: monochromatic LED lamp at 365 nm; photoirradiation time: 1 h. (B) Dependence of peak position on CO formation rate.

of the Ag–Co cocatalyst, as shown in Fig. S8.† These results clearly indicate that the residual MgO or $Mg(OH)_2$ on the surface of Mg–$SrTiO_3$ does not significantly improve the photocatalytic activity. Therefore, Mg^{2+}-doping into the bulk structure of $SrTiO_3$ is essential for good photocatalytic conversion of CO_2 in water.

Fig. 4 shows the XRD patterns of the Mg–$SrTiO_3$ fabricated by calcination at 1118, 1268, 1318, 1368, and 1418 K. These diffraction patterns correspond to the perovskite structure of $SrTiO_3$, and no impurity phases were observed in any of the cases. The position of the diffraction peak at 2θ = 68° in Fig. 4(A-2) is assigned to the (220) phase. This peak shifted to a lower angle with increasing calcination temperature, which indicates that Ti^{4+} in the bulk structure of $SrTiO_3$ was steadily replaced with Mg^{2+}. Therefore, Mg doping into $SrTiO_3$ can be enhanced by increasing the calcination temperature in the flux treatment. As shown in Fig. 5(A), Ag–Co/Mg–$SrTiO_3$_1118 K generated a small amount of CO during the photocatalytic reaction. Mg–$SrTiO_3$_1118 K can be considered as "undoped" $SrTiO_3$ because 1118 K is lower than the melting point of the $SrCl_2$ flux (1147 K). This is confirmed by the fact that the edge-shaved cubic structure was not observed in the SEM image of Mg–$SrTiO_3$_1118 K (Fig. S9†). Moreover, the CO formation rate drastically improved at the calcination temperature of 1268 K, which is higher than the melting point of the $SrCl_2$ flux. As shown in Fig. 5(B), a clear correlation was observed between the CO formation rate and the XRD peak positions, suggesting that greater doping amounts result in greater photocatalytic activity for the conversion of CO_2.

Fig. S10(A-1)† shows the XRD patterns of Mg–$SrTiO_3$_***y*** h, where ***y*** is the calcination time (***y*** = 1, 10, 15, and 20 h) for the doping process at 1418 K. The peak top position of the (220) phase shifted with increasing doping time, as shown in Fig. S10(A-2),† indicating that Mg doping into $SrTiO_3$ is enhanced by prolonging the doping time. Moreover, as shown in Fig. S11(B),† a positive correlation is observed between the photocatalytic activity for the conversion of CO_2 to CO and the peak top position of the (220) phase diffraction. These results confirm that the extent of Mg doping *via* the replacement of Ti^{4+} sites in $SrTiO_3$ with Mg^{2+} is a significant parameter for CO evolution.

Fig. S12† shows the XRD pattern of Mg(***z***)–$SrTiO_3$, where ***z*** is the molar ratio (mol%) of the Mg dopant to $SrTiO_3$ (***z*** = 0, 2, 4, 8, 24, and 100). Clear diffraction patterns corresponding to the perovskite structure of $SrTiO_3$ were observed in all cases. However, the diffraction patterns of Mg(0)–$SrTiO_3$ and Mg(2)–$SrTiO_3$ indicate a small impurity phase, which is attributed to Y_2O_3. This suggests that the Mg–$SrTiO_3$ samples were contaminated with the yttria crucible during their preparation. In contrast, a small diffraction peak corresponding to MgO was observed for Mg(24)–$SrTiO_3$ and Mg(100)–$SrTiO_3$, which is ascribed to excess amounts of the corresponding Mg dopants. The diffraction peak corresponding to the (220) facets of Mg(4)–$SrTiO_3$ appeared at a lower angle than that of the pristine sample, whereas the peak top position of Mg(8)–$SrTiO_3$ slightly shifted to a higher angle than that of Mg(4)–$SrTiO_3$. We attribute the former case to the replacement of Ti^{4+} sites of $SrTiO_3$ with Mg^{2+} species and the latter case to the replacement of some Sr^{2+} sites with Mg^{2+} species.

Fig. 6 shows the photocatalytic activity of Ag–Co/Mg(***z***)–$SrTiO_3$ in the conversion of CO_2 in water. Ag–Co/Mg(0)–$SrTiO_3$ exhibited negligible activity, and no product evolution was observed. However, the CO formation rate increased with increasing amounts of Mg dopants. The highest CO formation rates were observed for Ag–Co/Mg(4)–$SrTiO_3$ and Ag–Co/Mg(8)–$SrTiO_3$. These rates decreased slightly upon

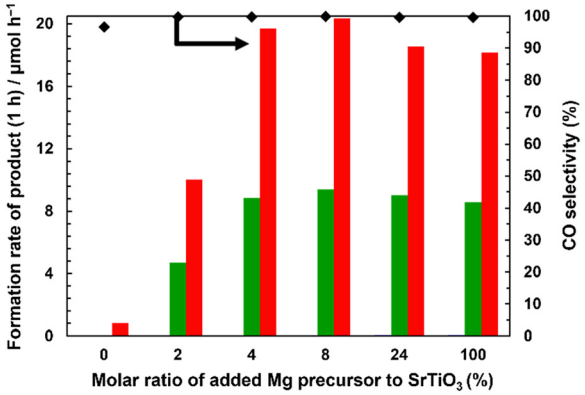

Fig. 6 Formation rates of CO (red), H_2 (blue), and O_2 (green) and selectivity toward CO evolution (black diamond) in the photocatalytic conversion of CO_2 in H_2O over the Ag–Co/Mg(**z**)–$SrTiO_3$ photocatalysts (**z** = 0, 2, 4, 8, 24, and 100). Reaction conditions: amount of photocatalyst: 0.2 g; Ag loading: 1 wt%; Co loading: 0.3 wt%; volume of reaction solution (H_2O): 0.2 L; additive: 0.1 M $NaHCO_3$; CO_2 flow rate: 30 mL min^{-1}; light source: monochromatic LED lamp at 365 nm; photoirradiation time: 1 h.

addition of excess Mg dopant, suggesting that 4 mol% of Mg dopant is optimal for CO evolution. Furthermore, our results suggest that the replacement of the Sr^{2+} sites with Mg^{2+} species and the presence of precipitated MgO do not influence the photocatalytic activity for the conversion of CO_2. Table S1† shows the actual atomic content of Sr, Ti, and Mg in Mg–$SrTiO_3$, Mg–$SrTiO_3$_1268 K, and Mg(2)–$SrTiO_3$ determined by ICP measurements. As we concluded in the above discussion, the formation rate of CO had a good agreement with the amount of Mg doped into $SrTiO_3$.

Fig. S13† shows the results of the control experiments for the photocatalytic conversion of CO_2 in water using optimised Ag–Co/Mg–$SrTiO_3$. The reduction of CO_2 to CO did not proceed well in the absence of the photocatalyst, photoirradiation, or the $NaHCO_3$ additive. These results clearly indicate that the presence of Ag–Co/Mg–$SrTiO_3$ photocatalyst and $NaHCO_3$ additive under UV-LED photoirradiation significantly enhanced the conversion of CO_2 to CO.[51] To confirm the origin of the evolved CO in the photocatalytic conversion of CO_2 in the presence of Ag–Co/Mg–$SrTiO_3$, we conducted isotope-labelling experiments using $^{13}CO_2$ gas as the substrate. Fig. 7 shows the gas chromatography-thermal conductivity detector (GC-TCD) chromatogram and the quadrupole mass spectrometer (Q-MS) profiles of m/z = 28 and 29 in the online GC-MS analysis for the photocatalytic conversion of $^{13}CO_2$. In the TCD-GC chromatogram, H_2 and O_2 were observed at 2 and 4 min, respectively, in addition to N_2 from air. Q-MS analysis of the outlet gas revealed no quantifiable peak at m/z = 28 except for N_2 contamination. In contrast, a clear peak appeared at approximately 19 min in the Q-MS profile of m/z = 29, indicating that ^{13}CO was produced from the introduced $^{13}CO_2$. This isotopic experiment confirmed that ^{13}C-labeled CO (m/z = 29) evolved preferentially over ^{12}CO (m/z = 28). This suggests that the evolved CO gas originated from the CO_2 gas

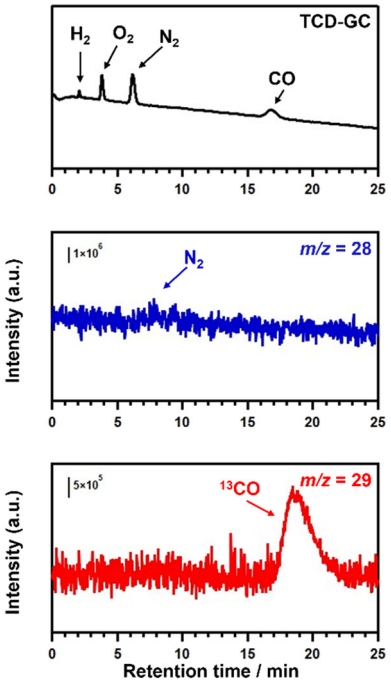

Fig. 7 Gas chromatography-thermal conductivity detector (GC-TCD) chromatogram and Q-MS profiles at m/z = 28 and 29 for the photocatalytic conversion of $^{13}CO_2$ in H_2O over Ag–Co/Mg–$SrTiO_3$. Reaction conditions: amount of photocatalyst: 0.2 g; Ag loading: 1 wt%; Co loading: 0.3 wt%; volume of reaction solution (H_2O): 0.2 L; additive: 0.1 M $NaHCO_3$; $^{13}CO_2$ flow rate: 30 mL min^{-1}; light source: monochromatic LED lamp at 365 nm; photoirradiation time: 1.5 h.

bubbled into the suspension. Furthermore, the apparent quantum efficiency (AQE) of optimal Mg–$SrTiO_3$ in the photocatalytic conversion of CO_2 using Ag–Co/Mg–$SrTiO_3$ photocatalyst under monochromatic UV-light irradiation (365 nm) was determined to be 0.05% (see ESI† for the details).

Scheme 1 shows the proposed mechanism for the photocatalytic conversion of CO_2 over Ag–Co/Mg–$SrTiO_3$ with

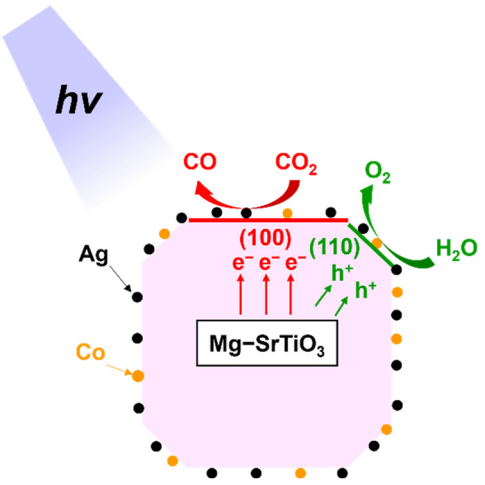

Scheme 1 Proposed mechanism of the photocatalytic conversion of CO_2 in H_2O over Ag–Co/Mg–$SrTiO_3$.

H_2O as the electron donor. As mentioned previously, a Mg–$SrTiO_3$ particle has an edge-shaved cube with exposed {100} and {110} facets. We inferred that the photocatalytic conversion of CO_2 to CO occurs at the Ag sites on the {100} facets of Mg–$SrTiO_3$, whereas oxidation of H_2O to O_2 proceeds at the Co sites on the {110} facets.[13,52] As shown in Fig. S14,† highly selective CO formation was observed continuously for 15 h despite the aggregation of the Ag nanoparticles owing to the photoirradiation (Fig. S15†).

Conclusions

An Mg-doped $SrTiO_3$ photocatalyst (Mg–$SrTiO_3$) was successfully synthesised using a previously reported flux method. Mg–$SrTiO_3$ exhibited excellent photocatalytic activity under monochromatic UV-light irradiation at 365 nm, resulting in selective conversion of CO_2 to CO in the presence of Ag–Co cocatalyst. The AQE of this reaction was determined to be 0.05%. Moreover, isotope experiments revealed that the evolved CO originated from gaseous CO_2. The CO formation rate drastically improved by doping Mg into $SrTiO_3$. SEM images of Mg–$SrTiO_3$ revealed the presence of edge-shaved cubic particles with {110} facets in addition to {100} facets. This was correlated to the separation of photogenerated carriers and consequent suppression of charge recombination, which dramatically improved the photocatalytic activity for the conversion of CO_2 to CO.

Author contributions

T. Nakamoto: investigation, writing – original draft preparation; S. Iguchi and S. Naniwa: visualization, writing – editing; T. Tanaka and K. Teramura: visualization, supervision, funding acquisition.

Conflicts of interest

There are no conflicts to declare.

Acknowledgements

This research was partially supported by the Program for Elements Strategy Initiative for Catalysts and Batteries (ESICB) commissioned by the Ministry of Education, Culture, Sports, Science, and Technology (MEXT) of Japan. This work was also supported by JSPS KAKENHI grants (21H01716 and 22K14541) and a Research Grant against Global Warming from the Ichimura Foundation for New Technology. The XAS measurements were performed at the BL14B2 of SPring-8 with the approval of the Japan Synchrotron Radiation Research Institute (JASRI) (Proposal No. 2022B1885).

References

1 A. H. Xie, J. P. Zhu, S. C. Kang, X. Qin, B. Xu and Y. C. Wang, *Sci. Rep.*, 2022, **12**, 16548.
2 J. F. B. Mitchell, *Rev. Geophys.*, 1989, **27**, 115–139.
3 P. M. Cox, R. A. Betts, C. D. Jones, S. A. Spall and I. J. Totterdell, *Nature*, 2000, **408**, 184–187.
4 Y. Kuzyakov, W. R. Horwath, M. Dorodnikov and E. Blagodatskaya, *Soil Biol. Biochem.*, 2019, **128**, 66–78.
5 P. R. Yaashikaa, P. S. Kumar, S. J. Varjani and A. Saravanan, *J. CO2 Util.*, 2019, **33**, 131–147.
6 M. W. Yuan, M. J. Kummer and S. D. Minteer, *Chem. – Eur. J.*, 2019, **25**, 14258–14266.
7 M. G. Kibria, J. P. Edwards, C. M. Gabardo, C. T. Dinh, A. Seifitokaldani, D. Sinton and E. H. Sargent, *Adv. Mater.*, 2019, **31**, 1807166.
8 A. Fujishima and K. Honda, *Nature*, 1972, **238**, 37–38.
9 Q. Wang, J. Warnan, S. Rodriguez-Jimenez, J. J. Leung, S. Kalathil, V. Andrei, K. Domen and E. Reisner, *Nat. Energy*, 2020, **5**, 703–710.
10 Y. Nosaka, S. Takahashi, Y. Mitani, X. Q. Qui and M. Miyauchi, *Appl. Catal., B*, 2012, **111–112**, 636–640.
11 Z. D. Liu and Z. Ma, *Mater. Res. Bull.*, 2019, **118**, 110492.
12 M. Siebenhofer, A. Viernstein, M. Morgenbesser, J. Fleig and M. Kubicek, *Mater. Adv.*, 2021, **2**, 7583–7619.
13 Y. Ham, T. Hisatomi, Y. Goto, Y. Moriya, Y. Sakata, A. Yamakata, J. Kubota and K. Domen, *J. Mater. Chem. A*, 2016, **4**, 3027–3033.
14 T. Takata, J. Z. Jiang, Y. Sakata, M. Nakabayashi, N. Shibata, V. Nandal, K. Seki, T. Hisatomi and K. Domen, *Nature*, 2020, **581**, 411–414.
15 K. Kato, J. Z. Jiang, Y. Sakata and A. Yamakata, *ChemCatChem*, 2019, **11**, 6349–6354.
16 J. Z. Jiang, K. Kato, H. Fujimori, A. Yamakata and Y. Sakata, *J. Catal.*, 2020, **390**, 81–89.
17 J. J. Yang, Y. Zhang, X. Y. Xie, W. H. Fang and G. L. Cui, *ACS Catal.*, 2022, **12**, 8558–8571.
18 J. Albero, Y. Peng and H. Garcia, *ACS Catal.*, 2020, **10**, 5734–5749.
19 C. Zhou, J. Zhou, L. Lu, J. Wang, Z. Shi, B. Wang, L. Pei, S. Yan, Y. Zhentao and Z. Zou, *Appl. Catal., B*, 2018, **237**, 742–752.
20 Y. Liu, F. B. Yu, F. Wang, S. J. Bai and G. W. He, *Chin. J. Struct. Chem.*, 2022, **41**, 2201034–2201039.
21 S. Rodriguez-Jimenez, H. W. Song, E. Lam, D. Wright, A. Pannwitz, S. A. Bonke, J. J. Baumberg, S. Bonnet, L. Hammarstrom and E. Reisner, *J. Am. Chem. Soc.*, 2022, **144**, 9399–9412.
22 J. Li, Y. L. He, L. Tan, P. P. Zhang, X. B. Peng, A. Oruganti, G. H. Yang, H. Abe, Y. Wang and N. Tsubaki, *Nat. Catal.*, 2018, **1**, 787–793.
23 K. Teramura, H. Tatsumi, Z. Wang, S. Hosokawa and T. Tanaka, *Bull. Chem. Soc. Jpn.*, 2015, **88**, 431–437.
24 Z. Wang, K. Teramura, S. Hosokawa and T. Tanaka, *Appl. Catal., B*, 2015, **163**, 241–247.
25 S. Iguchi, K. Teramura, S. Hosokawa and T. Tanaka, *Catal. Sci. Technol.*, 2016, **6**, 4978–4985.
26 R. Pang, K. Teramura, H. Asakura, S. Hosokawa and T. Tanaka, *Appl. Catal., B*, 2017, **218**, 770–778.
27 Z. Wang, K. Teramura, Z. Huang, S. Hosokawa, Y. Sakata and T. Tanaka, *Catal. Sci. Technol.*, 2016, **6**, 1025–1032.
28 J. L. White, M. F. Baruch, J. E. Pander, Y. Hu, I. C. Fortmeyer, J. E. Park, T. Zhang, K. Liao, J. Gu, Y. Yan, T. W. Shaw, E. Abelev and A. B. Bocarsly, *Chem. Rev.*, 2015, **115**, 12888–12935.

29 H. Cho, W. D. Kim, J. Yu, S. Lee and D. C. Lee, *ChemCatChem*, 2018, **10**, 5679–5688.
30 X. Zhu, A. Yamamoto, S. Imai, A. Tanaka, H. Kominami and H. Yoshida, *Appl. Catal., B*, 2020, **274**, 119085.
31 G. Yang, M. Lu, J. Xiong and G. Cheng, *J. Alloys Compd.*, 2022, **909**, 164792.
32 S. Wang, K. Teramura, T. Hisatomi, K. Domen, H. Asakura, S. Hosokawa and T. Tanaka, *Chem. Sci.*, 2021, **12**, 4940–4948.
33 M. Takemoto, Y. Tokudome, S. Kikkawa, K. Teramura, T. Tanaka, K. Okada, H. Murata, A. Nakahira and M. Takahashi, *RSC Adv.*, 2020, **10**, 8066–8073.
34 X. W. Xu, K. Teramura, H. Asakura, S. Hosokawa and T. Tanaka, *Appl. Catal., B*, 2021, **298**, 120508.
35 R. Pang, K. Teramura, M. Morishita, H. Asakura, S. Hosokawa and T. Tanaka, *Commun. Chem.*, 2020, **3**, 137.
36 K. Iizuka, T. Wato, Y. Miseki, K. Saito and A. Kudo, *J. Am. Chem. Soc.*, 2011, **133**, 20863–20868.
37 L. Pei, Z. Xu, Z. Shi, H. Zhu, S. C. Yan and Z. G. Zou, *J. Mater. Chem. A*, 2017, **5**, 20439–20447.
38 S. Y. Wang, K. Teramura, T. Hisatomi, K. Domen, H. Asakura, S. Hosokawa and T. Tanaka, *ACS Appl. Energy Mater.*, 2020, **3**, 1468–1475.
39 Y. Liu, L. Xie, Y. Li, R. Yang, J. L. Qu, Y. Q. Li and X. G. Li, *J. Power Sources*, 2008, **183**, 701–707.
40 R. D. Shannon, *Acta Crystallogr., Sect. A: Cryst. Phys., Diffr., Theor. Gen. Crystallogr.*, 1976, **32**, 751–757.
41 H. Yu, J. J. Wang, S. C. Yan, T. Yu and Z. G. Zou, *J. Photochem. Photobiol., A*, 2014, **275**, 65–71.
42 C. Zhang, Y. Z. Jia, Y. Jing and Y. Yao, *Int. J. Hydrogen Energy*, 2015, **40**, 1343–1351.
43 F. T. Wagner and G. A. Somorjai, *J. Am. Chem. Soc.*, 1980, **17**, 5494–5502.
44 C. L. Haynes and R. P. Van Duyne, *J. Phys. Chem. B*, 2001, **105**, 5599–5611.
45 M. Nakabayashi, T. Takata, N. Shibata and K. Domen, *Chem. Lett.*, 2022, **51**, 978–981.
46 R. Pang, K. Teramura, H. Asakura, S. Hosokawa and T. Tanaka, *ACS Sustainable Chem. Eng.*, 2019, **7**, 2083–2090.
47 Z. Huang, K. Teramura, H. Asakura, S. Hosokawa and T. Tanaka, *J. Mater. Chem. A*, 2017, **5**, 19351.
48 M. A. Avila-Lopez, E. Luevano-Hipolito and L. M. Torres-Martinez, *J. Photochem. Photobiol., A*, 2019, **382**, 111933.
49 W. K. Jo, S. Kumar and S. Tonda, *Composites, Part B*, 2019, **176**, 107212.
50 S. Iguchi, Y. Hasegawa, K. Teramura, S. Kidera, S. Kikkawa, S. Hosokawa, H. Asakura and T. Tanaka, *Sustainable Energy Fuels*, 2017, **1**, 1740–1747.
51 K. Teramura, K. Hori, Y. Terao, Z. Huang, S. Iguchi, Z. Wang, H. Asakura, S. Hosokawa and T. Tanaka, *J. Phys. Chem. C*, 2017, **121**, 8711–8721.
52 A. Yamakata, M. Kawaguchi, N. Nishimura, T. Minegishi, J. Kubota and K. Domen, *J. Phys. Chem. C*, 2014, **118**, 23897–23906.